38th Fluid Dynamics Conference and Exhibit
23 - 26 June 2008, Seattle, Washington

AIAA 2008-4303

38th AIAA Fluid Dynamics Conference, Jun 23-26, 2008, Seattle, WA

Reynolds Number Effects on Cone Forebody Side Force

Xuanshi Meng*, Zhide Qiao†, Chao Gao‡
Northwestern Polytechnical University, Xi'an 710072, China
Shijun Luo§, and Feng Liu¶
University of California, Irvine, CA 92697-3975

This paper reports results from comprehensive pressure measurements of a circular cone-cylinder model in a low-turbulence $3.0 \times 1.6\ m$ low-speed wind tunnel. The semi-apex angle of the cone is 10°. The results consist of detailed pressure distributions over nine stations on the cone at 35° angle of attack and free-stream Reynolds number of $(0.1 - 0.9) \times 10^6$ based on the cone base diameter. The tests encompassed a complete coverage of roll angles in 9° intervals. Local and overall forces and moments are calculated from the measured pressures. The variation of local side-force coefficient normalized by the local diameter of the cone, with roll angle is nearly a square-wave curve. At $Re = (0.7, 0.9) \times 10^6$, the maximum side force is reduced, which is caused by late separation of the boundary layer, and irregular values of side force occur at a few roll angles, which is correlated to disagreement of separation asymmetry with pressure asymmetry. Important asymmetry features which are valid for all of the Reynolds numbers are clarified.

Nomenclature

C_m	=	pitching-moment coefficient about cone base, pitching moment/$q_\infty SD$
C_n	=	yawing-moment coefficient about cone base, yawing moment/$q_\infty SD$
C_{Nd}	=	local normal force coefficient, local normal force/$q_\infty d$
C_{N0}	=	overall normal force coefficient, overall normal force/$q_\infty S$
C_{Yd}	=	local side force coefficient, local side force/$q_\infty d$
C_{Y0}	=	overall side force coefficient, overall side force/$q_\infty S$
c_p	=	pressure coefficient
D	=	base diameter of circular cone
d	=	local diameter of circular cone
L	=	length of circular cone
M	=	free-stream Mach number
q_∞	=	free-stream dynamic pressure
Re	=	free-stream Reynolds number based on D
S	=	base area of circular cone

*Graduate Student, Department of Fluid Mechanics.
†Professor, Department of Fluid Mechanics.
‡Professor and Associte Director, Aerodynamic Design and Research National Laboratory.
§Researcher, Department of Mechanical and Aerospace Engineering.
¶Professor, Department of Mechanical and Aerospace Engineering. Associate Fellow AIAA.

V	=	free-stream velocity
x, y, z	=	body axes, Fig. 5
α	=	angle of attack
θ	=	meridian angle measured from windward generator, Fig. 5
$\Delta\theta_w$	=	wake angle, i.e., meridian angle interval covered by wake
θ_w	=	meridian angle of the wake center
ϕ	=	roll angle

I. Introduction

Symmetric separation vortices over a slender pointed body of revolution may become asymmetric as the angle of attack is increased beyond a certain value, causing asymmetric force and moment even at symmetric flight conditions.[1] Reynolds number Effects on high angle of attack aerodynamics are complicated by the presence of complex separated flow structures. The understanding and quantification of such flow effects remains a substantial challenge to the design of modern aircraft and missiles. The subject has been reviewed by Haines[2] and Munro et al.[3]

Reynolds number effect research has been focused on ogive cylinder. The maximum side force is reduced in the transitional separation regime as shown by Lamont[4] using comprehensive pressure tests. The flow-field and surface-flow field patterns over ogive forebody were observed by Keener[5] using several flow-visualization methods. Reynolds number significantly affects the extent of primary laminar, tansitional, and turbulent boundary-layer separations. Hall[6] compared, for ogive forebodies with fineness ratios of 3.5, flow patterns from the oil-flow photographs obtained by Keener to features in pressure distributions measured by Lamont and revealed that the primary character of the separation can be determined from either the oil-flow photos or from the pressure data. According to Poll,[7] the mechanisms for boundary-layer transition on a cylindrical afterbody at incidence in low-speed flow are: (1) free shear layer instability (i.e. transition in a laminar separation bubble), (2) contamination along the attachment line, (3) cross-flow instability, (4) streamwise-flow (Tollmein-Schlichting) instability.

There seems little doubt that the apex of the pointed slender body plays a decisive role in determining the flow pattern over the entire body. Since the pointed nose is locally conical in shape, the flow may be regarded as locally equivalent to that about a tangent cone. The basic features of the asymmetric flow about pointed slender bodies of revolution can be displayed by studying the flows over a circular cone.

Pressure distributions over a circular cone at high angles of attack were studied. Moskovitz et al.[8] measured pressures at three sections on the nose cone at the Reynolds number of 8.4×10^4. Fiddes[9] gave measured pressures at one front section at the Reynolds number of 0.9×10^6. Meng, et al.[10] conducted comprehensive pressure tests at the Reynolds number of 0.3×10^6 with a complete coverage of roll orientations. Asymmetry over the cone forebody develops in three angle-of-attack stages: $10^\circ - 20^\circ$–symmetric separation with no side force, $20^\circ - 35^\circ$–asymmetric separation with side force varying with roll angle as continuous-wave curve, and 35°–asymmetric separation with side force varying with roll angle as square-wave curve.

The present paper studies the Reynolds number effects on cone forebody side force. In the following sections, the experimental setup is described and verified by measurements at zero angle of attack. The Reynolds-number effects on the local side force variation with roll and along cone length are identified. The mechanisms for the effects are analyzed with the boundary-layer separation states inferred from the measured pressures. The general mechanism for pressure asymmetry is examined. The results are confirmed by available data in the literature. Conclusions are lastly offered.

II. Experimental Setup

The tests are conducted in the NF-3 wind tunnel at the Aerodynamic Design and Research National Laboratory, Northwestern Polytechnical University. The test section has a $3.0 \times 1.6\ m$ cross section, and a length of $8.0\ m$. The contraction ratio is $20 : 1$. The free-stream turbulence level is 0.045% for wind speeds of $20 \sim 130\ m/s$. The model comprises a nose cone of 10° semi-apex angle faired to a cylindrical afterbody as shown in Fig. 1.

The tip portion of the cone of $150.0\ mm$ in length is separately made to facilitate the pressure-tube

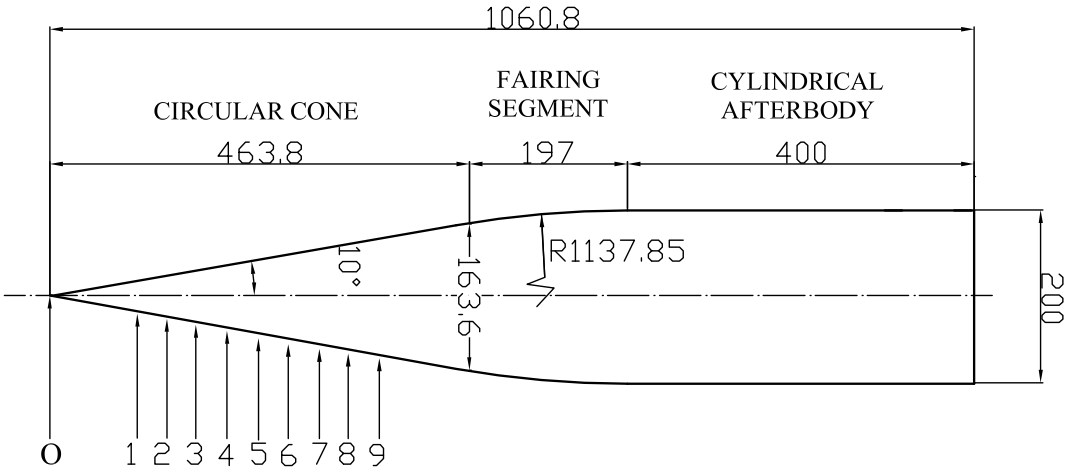

O—1	O—2	O—3	O—4	O—5	O—6	O—7	O—8	O—9
98.5	133.2	166.8	201.9	236.9	272.0	307.1	342.1	377.2

DIMENSIONS IN mm

Figure 1. The cone-cylinder model.

installation inside the model. After assembling the tip with the rest of the model, the junction was filled with grease and polished. The model is made of metal and constructed to an average tolerance of $\pm 0.05\ mm$ with a surface finish of nearly $\pm 0.8\ \mu m$. The fore-body including the nose cone and the fairing portion is roll-able and the after cylinder is mounted onto the model support. The junction between the fore-body and the after cylinder is carefully machined so that the surface discontinuity is less than $0.025\ mm$.

The fore-body's roll orientation is facilitated by clamping the fore-body to the axis of a remotely controlled motor.The model can be set at any roll angle between 0 and 351° from the chosen datum in 9° intervals. The accuracy of the roll-angle set is about 1%. The pressure instrumentation is confined to the nose cone and is well forward of the model support. The pressure tapings are placed at 9 stations along the model's axis as shown in Fig. 1. Stations 1 and 2 have 12 and 18 pressure orifices, respectively, and the rest stations have 36 pressure orifices. The pressure orifices in each station are equally-spaced around the circumference and arranged from the same datum for all stations. The total number of the pressure orifices is 282.

The static pressure at the each pressure orifice is transmitted by a rubber tube passing through the base of the afterbody to the pressure-measurement system outside the test section. The system consists of 24 scan-valves each of which has 16 channels and one pressure transducer of modulus 9816 of the PSI Company with an accuracy of $\pm 0.05\%$. The pressure-measurement readings for each test case were taken 115 times in $0.05\ s$ intervals and then time-averaged. The fluctuations of the readings are small and the time-averaged data are meaningful. A thorough job of cleaning the model was done prior to each run of the wind tunnel. Figure 2 shows the test model rigidly supported in the wind tunnel.

The experimental setup is verified by measured pressures at zero angle of attack. Figure 3 presents the pressure coefficient c_p versus θ at $\alpha = 0°$ and $\phi = 0$ for all stations, and $V = 30\ m/s$. The maximum variation of c_p with θ is generally less than 0.01 on each station except the two front stations. The maximum variation of 0.2 on Station 2 at $\theta = 350°$ may be caused by uncareful handling of the model. Figure 4 presents the pressure coefficient c_p at Orifice 1 versus ϕ at $\alpha = 0°$ for all stations, and $V = 30\ m/s$. Orifice 1 is located at $\theta = 230°$ when $\phi = 0°$. The maximum variation of c_p with ϕ is also smaller than 0.01 on all stations. Figs. 3 and 4 verify that the model is axi-asymmetric and the model axis parallels with the free-stream velocity at this angle of attack for all roll angles.

The cone-cylinder model is tested at $\alpha = 35°$, $V = 10, 30, 50, 70, 80\ m/s$, $M = 0.03 - 0.24$ and $Re = (0.1 - 0.9) \times 10^6$. 40 roll orientations in 9° intervals are tested. A few readings of the measured pressure are

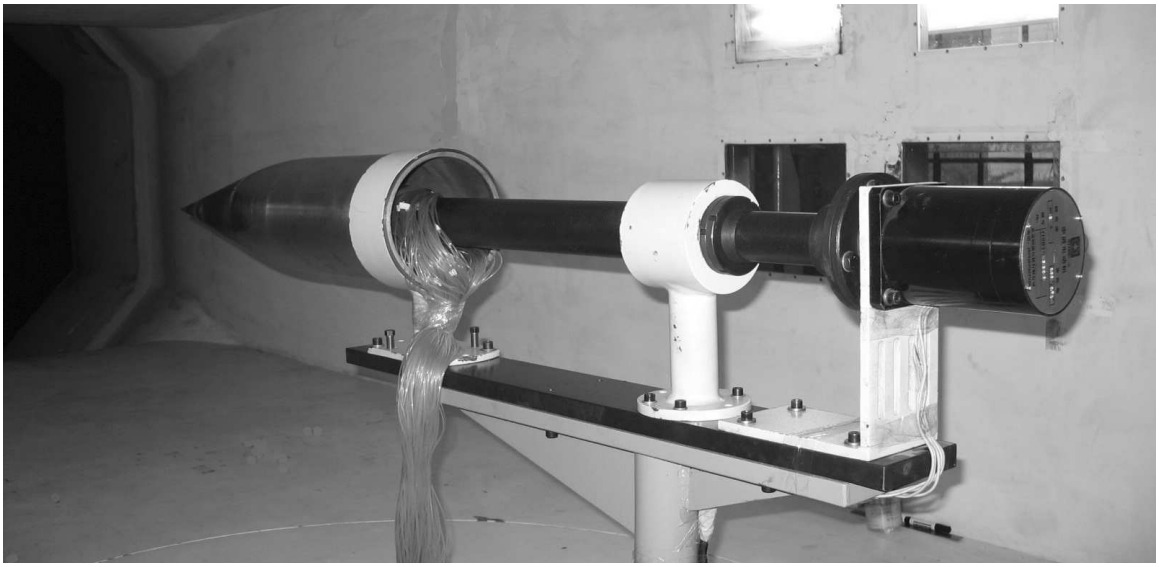

Figure 2. The model in the wind tunnel.

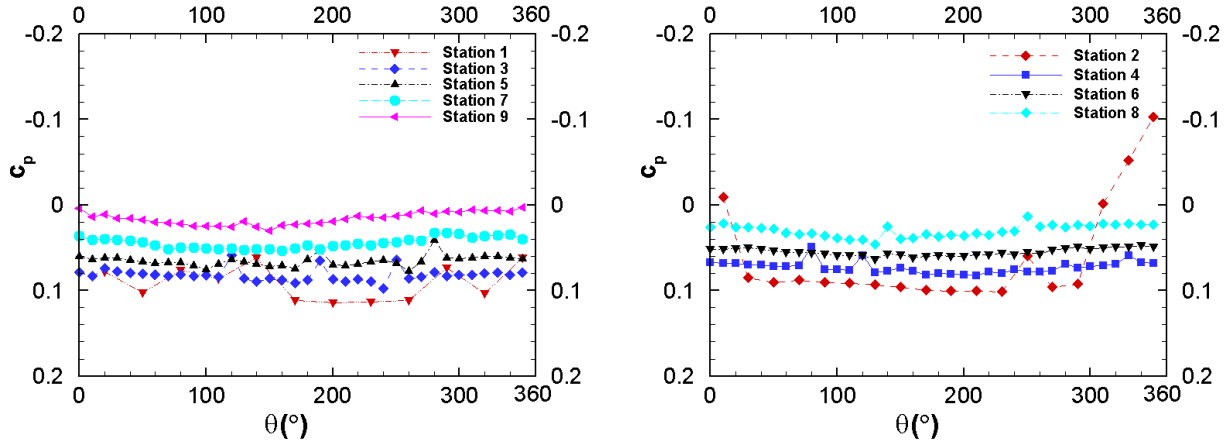

(a) Odd-numbered stations

(b) Even-numbered stations

Figure 3. Pressure coefficient vs. θ at $\alpha = 0°$, $\phi = 0$ and $V = 30\ m/s$.

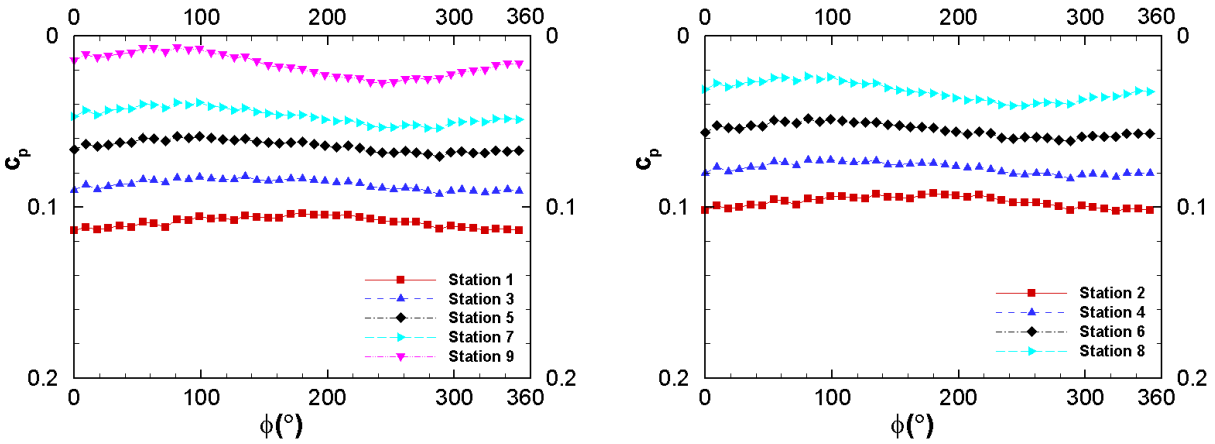

(a) Odd-numbered stations (b) Even-numbered stations

Figure 4. Pressure coefficient vs. ϕ at $\alpha = 0°$, Orifice 1 and $V = 30\ m/s$.

abnormal in the tests at certain roll orientations due to the twisting of the bunch of the 282 pressure tubes during the fore-body roll. The corrected pressure coefficient is calculated with linear interpolation from the neighboring normal values.

III. $C_{Yd}(\phi)$ and $C_{Nd}(\phi)$ at Various Reynolds Numbers

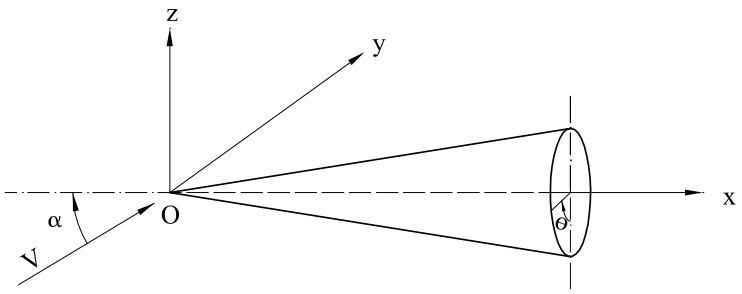

Figure 5. Body axes of the circular cone at an angle of attack.

The measured pressures are integrated to give side- and normal-forces in the body axes shown in Fig. 5, where the coordinate plane Oxz coincides with the incidence plane. The local side- and normal-force coefficients, C_{Yd} and C_{Nd} are based on the local diameter d rather than the base diameter D, in order to confer more information as shown by Hall.[11]

Figure 6 presents the local side- and normal-force coefficients C_{Yd} and C_{Nd} versus roll angle ϕ at Station 3 for various Reynolds numbers. The curves $C_{Yd}(\phi)$ are nearly a square wave having two cycles. The side force takes either the maximum positive value or the maximum negative value. The positive and negative extremes would have to be of the same magnitude (approximately 0.6) since the model is axi-symmetric and was set in a symmetric flight. The small deviation may be caused by micro asymmetries in the experimental setup. There appear usually one irregular value between the regular extremes when the side force experiences a zero crossing. For $Re = 0.7 \times 10^6$, there are extra irregular local side forces in the two ranges of roll angle:

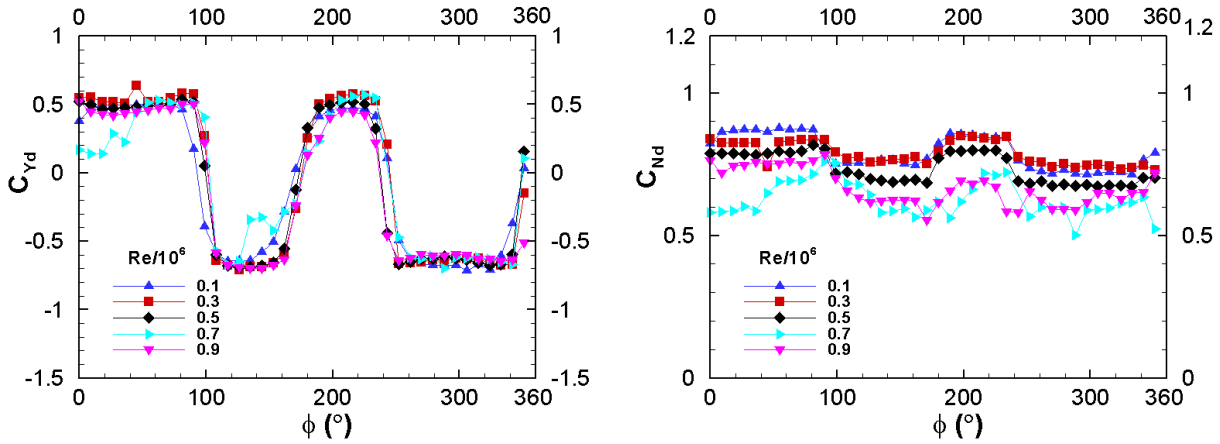

(a) Local side-force coefficient (b) Local normal-force coefficient

Figure 6. Local side- and normal-force coefficients vs. ϕ at Station 3 for various Reynolds numbers.

$\phi = 0° - 36°$ (5 points) and $135° - 198°$ (8 points). For $Re = 0.9 \times 10^6$, there appear two extra irregular local side-forces at $\phi = 180°$ and 189°. The local normal-force coefficient is nearly invariant with roll angle and has the same order of magnitude as the maximum local side-force coefficient.

The maximum local side force coefficient and the corresponding pressure distribution at Station 3 obtained at $Re = 0.9 \times 10^6$ in the present tests are nearly identical to those determined by Fiddes[9] under about the same test conditions.[12] This indicates that the maximum local side force determined for one model could be applied to models having the same apex angle under the same flow conditions. However, the pattern of the curve $C_{Yd}(\phi)$ in Figure 6 can have no general applications, since micro surface imperfections are random. For example, Moskovitz et al.[8] recorded square-wave curve at $\alpha = 40°$ which has two cycles but different pattern from Figure 6. The result of Fiddes[9] obtained under about the same flow conditions has three cycles entirely different from the present.

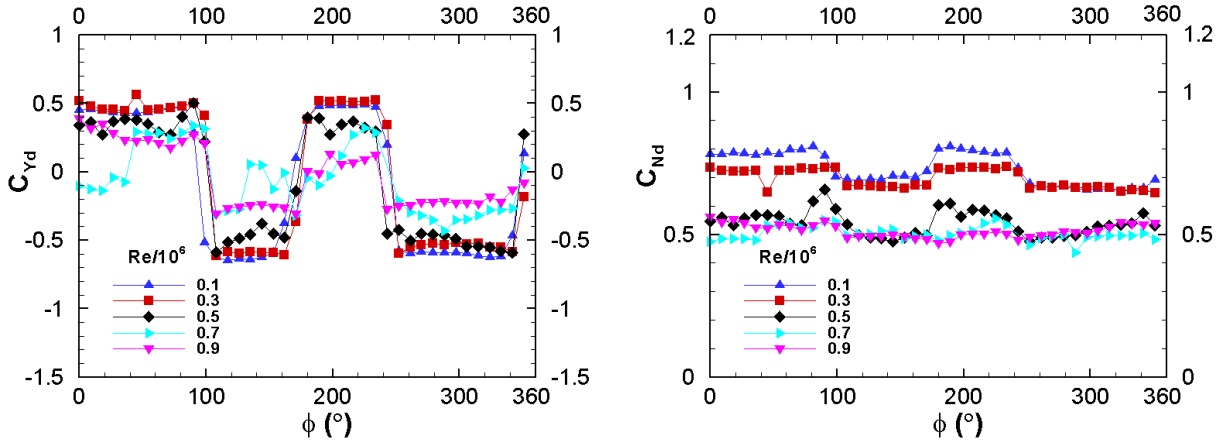

(a) Local side-force coefficient (b) Local normal-force coefficient

Figure 7. Local side- and normal-force coefficients vs. ϕ at Station 9 for various Reynolds numbers.

Figure 7 presents the local side- and normal-force coefficients C_{Yd} and C_{Nd} versus roll angle ϕ at Station 9 for various Reynolds numbers. The square-wave curve patterns are similar. The Reynolds number effects are evident at $Re = (0.7, 0.9) \times 10^6$ on all stations:

1. The maximum value of local side force is significantly reduced along the cone length.

2. Irregular local side force occurs at a few roll angles. Table 1 gives the roll angles at which irregular

local side force occurs.

Table 1. Roll angle ϕ at which irregulr local side force occurs on all stations at $Re = (0.7, 0.9) \times 10^6$.

$Re/10^6$	ϕ
0.7	$0° - 36°$, $135° - 198°$
0.9	$180°, 189°$

IV. Boundary-Layer Separation States at Various Reynolds Numbers

Boundary-layer states of the cross flow at variour Reynolds numbers are investigated. Although no flow field surveys were made in the present tests, the primary state of the boundary layer separation can be inferred from the measured pressures as shown by Hall.[6] The pressure-measurement orifices on all of the stations except the front two stations would be dense enough to yield the primary picture of the cross flow. It should be noted that it is difficult to construct the correct vortex configuration from the surface pressure distributions. Sometimes, there is no clear indication for locating nearby vortex. The interpretations given herein are to the best of the authors' knowledge. Figures 8, 9, 10, 11 and 12 present the measured pressure distribution and the inferred cross-flow streamline at Station 3 and $\phi = 0$ for $Re = (0.1, 0.3, 0.5, 0.7, 0.9) \times 10^6$, respectively, where P denotes suction peak point, S denotes separation point, and R denotes reattachment point. The first subscript 1 and 2 denote the specified point on port and starboard side, respectively. The second subscript 1 and 2 denote the first and second occurence of the specified point, respectively.

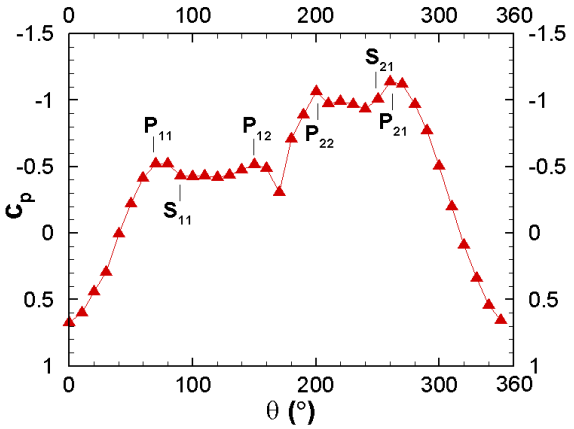

(a) Pressure coefficient

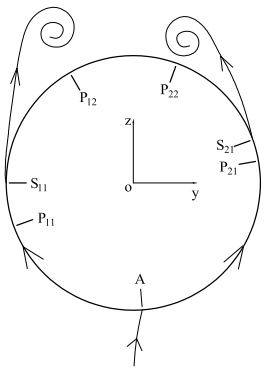

(b) Cross-flow streamline

Figure 8. Measured pressure and inferred cross-flow streamline at Station 3, $\phi = 0$, $Re = 0.1 \times 10^6$.

As shown in Figure 8(a) the sectional pressure distribution for $Re = 0.1 \times 10^6$ has two suction peaks and one separation point on each side of the cone. The first suction peaks P_{11} and P_{21} result directly from the convex shape of the circular cross-section. The second suction peaks P_{12} and P_{22} are induced by the vortex cores separated from the boundary layers of the port and starboard side, respectively. The suction peak P_{22} is higher than the suction peak P_{12}, which indicates that the starboard-side vortex core lies closer to the body surface than the port-side one. The higher suction peak P_{22} could delay the separation S_{21} and enhance the first suction peak P_{21} on the same side of the body. The asymmetric pressure distribution results in a local side force pointing to the starboard side of the section. The cross-flow streamline is inferred from the measured pressure and shown in Fig. 8(b). The separation points S_{11} and S_{21} are the origin of the feeding sheet of vorticity. The state of the boundary-layer separation is simply *laminar separation*, $\mathcal{LS}$ on both sides at this low Reynolds number.

For $Re = 0.3 \times 10^6$, Fig. 9(a) shows that there exists only one suction peak P_{11} on the port side and two suction peaks P_{21} and P_{22} on the starboard side. On the starboard side the first separation S_{21} is followed by a reattachment R_2 and then the second separation S_{22}. A transition occurs in the separation bubble

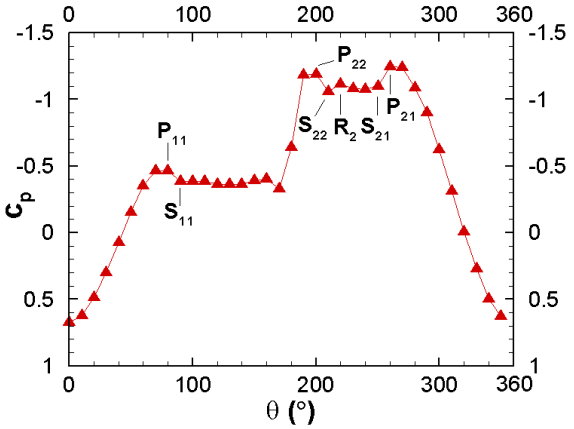

(a) Pressure coefficient

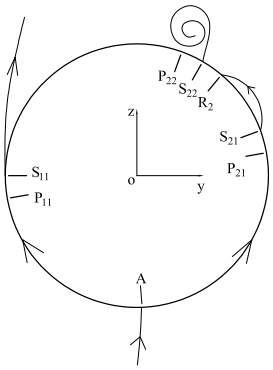

(b) Cross-flow streamline

Figure 9. Measured pressure and inferred cross-flow streamline at Station 3, $\phi = 0$, $Re = 0.3 \times 10^6$.

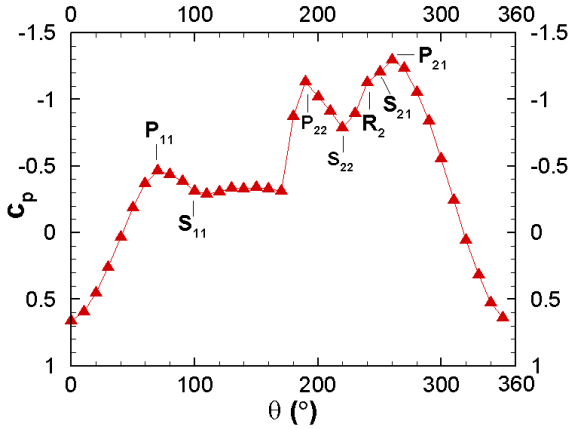

(a) Pressure coefficient

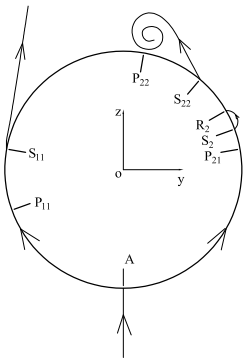

(b) Cross-flow streamline

Figure 10. Measured pressure and inferred cross-flow streamline at Station 3, $\phi = 0$, $Re = 0.5 \times 10^6$.

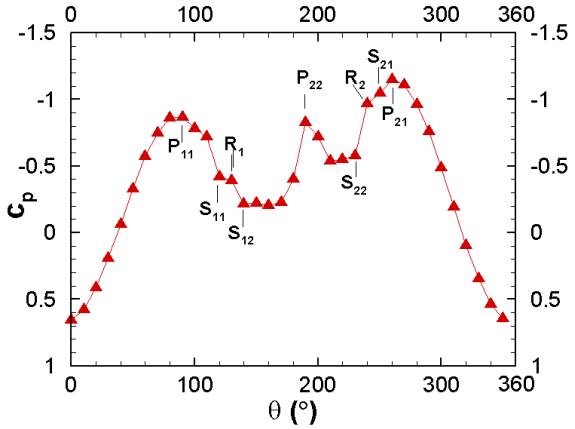

(a) Pressure coefficient

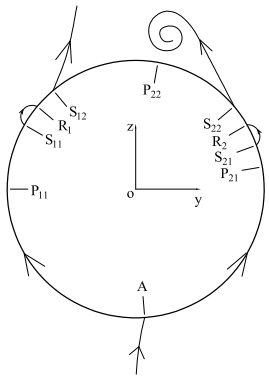

(b) Cross-flow streamline

Figure 11. Measured pressure and inferred cross-flow streamline at Station 3, $\phi = 0$, $Re = 0.7 \times 10^6$.

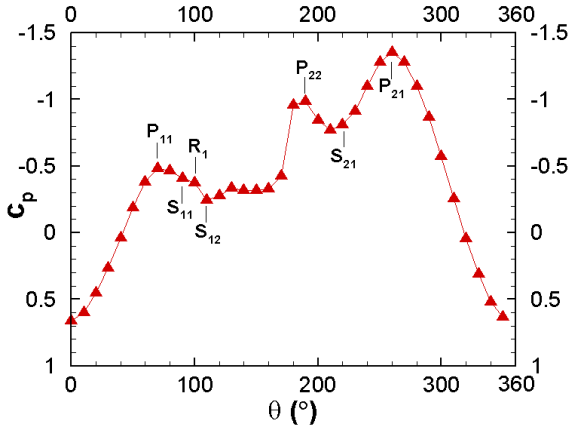

(a) Pressure coefficient

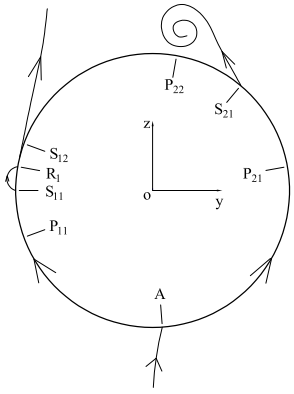

(b) Cross-flow streamline

Figure 12. Measured pressure and inferred cross-flow streamline at Station 3, $\phi = 0$, $Re = 0.9 \times 10^6$.

between S_{21} and R_2 caused by free shear layer instability. The state of the starboard-side boundary-layer separation is *laminar separation-transition in laminar bubble-turbulent reattachment-turbulent separation*, $\mathcal{TRS}$. The port-side state stays as $\mathcal{LS}$. The cross-flow streamline is inferred from the measured pressures and shown in Fig. 9(b). The separation points S_{11} and S_{22} are the origin of the feeding sheet of vorticity. The vortex separated from the starboard-side boundary layer would be lying nearby the section and the vortex separated from the port side would be remote from the body. For $Re = 0.5 \times 10^6$, the pattern of the pressure distribution and the inferred cross-flow streamline are similar to those for $Re = 0.3 \times 10^6$ as shown in Fig. 10.

For $Re = 0.7 \times 10^6$, the roll angle $\phi = 0^\circ$ yields an irregular side force on the square-wave curve of $C_{Yd}(\phi)$. Fig. 11 shows that the state of the boundary-layer separation on both side of the section is $\mathcal{TRS}$. The separation points S_{12} and S_{22} are the origin of the feeding sheet of vorticity. For $Re = 0.9 \times 10^6$ Fig. 12 shows that the separation state stays as $\mathcal{TRS}$ on the port side. On the starboard side the separation state is fully *turbulent separation*, $\mathcal{TS}$. The separation points S_{12} and S_{21} are the origin of the feeding sheet of vorticity. A transition on the starboard side would be caused by either cross-flow instability or streamwise flow instability of the laminar boundary layer.[7] For a circular-cone forebody the attachment-line flow would experience no adverse pressure gradient. The micro surface imperfections of the model act as instability trigger. Under a given Reynolds number the first occurrence of $\mathcal{TRS}$ or $\mathcal{TS}$ on the starboard side in the above cases may be due to the larger local flow speed on this side than the other side. Under the same small perturbations the separation state changes from $\mathcal{LS}$ to TRS, and then to $\mathcal{TS}$ as the Reynolds number increases.

Table 2. Meridian angle of characteristic points and separation state on port and starboard side, wake angle $\Delta\theta_w$, meridian angle of wake center θ_w and C_{Yd}, at $\phi = 0$, Station 3.

	Port side				*Starboard side*						
$Re/10^6$	S_{11}	R_1	S_{12}	*State*	S_{21}	R_2	S_{22}	*State*	$\Delta\theta_w$	θ_w	C_{Yd}
0.1	90°	*N/A*	*N/A*	$\mathcal{LS}$	−110°	*N/A*	*N/A*	$\mathcal{LS}$	160°	170°	0.38
0.3	90°	*N/A*	*N/A*	$\mathcal{LS}$	−110°	−140°	−150°	$\mathcal{TRS}$	120°	150°	0.54
0.5	100°	*N/A*	*N/A*	$\mathcal{LS}$	−110°	−120°	−140°	$\mathcal{TRS}$	120°	160°	0.52
0.7	120°	130°	140°	$\mathcal{TRS}$	−110°	−120°	−130°	$\mathcal{TRS}$	90°	<u>185°</u>	0.17
0.9	90°	100°	110°	$\mathcal{TRS}$	−140°	*N/A*	*N/A*	$\mathcal{TS}$	110°	165°	0.52

To summarize the above results, Table 2 presents the meridian angle of various separation points and the separation state on the port and starboard side, the wake angle $\Delta\theta_w$, the meridian angle of wake center θ_w and the local side-force coefficient C_{Yd} for various Reynolds numbers at Station 3 and $\phi = 0$, where the underline denotes that the wake center lies on the side to which the side force is pointed and thus the separation asymmetry disagrees with the pressure asymmetry. For $Re = 0.1 \times 10^6$ the wake angle is large ($\Delta\theta_w = 160^\circ$) because of the early separation of $\mathcal{LS}$. A large wake angle would provide space for developing high vortex asymmetry. The wake center is located on the port side ($\theta_w = 170^\circ$), which agrees with the local side force pointing to the starboard side ($C_{Yd} = 0.38$). For $Re = (0.3, 0.5, 0.9) \times 10^6$ the wake angles are moderate on Station 3, $\Delta\theta_w = 110^\circ - 120^\circ$. Their wake centers all lie on the port side ($\theta_w = 150^\circ - 165^\circ$) and agree with the positive local side forces ($C_{Yd} = 0.52 - 0.54$). For $Re = 0.7 \times 10^6$, the wake angle is small ($\Delta\theta_w = 90^\circ$) because of the late separation of $\mathcal{TRS}$ on both sides. A late separation would produce weak wake vortices and a low local side force. Although the local side force is pointing to the starboard side, the wake center is located on the starboard side ($\theta_w = 185^\circ$). The separation asymmetry disagrees with the pressure asymmetry. This disagreement restrains the production of pressure asymmetry and produces low side force, $C_{Yd} = 0.17$.

At the irregular points of $C_{Yd}(\phi)$, besides the wake angle is small ($\Delta\theta_w \approx 90^\circ$), the separation asymmetry may disagree with the corresponding pressure asymmetry at certain roll angles, e.g., $\phi = 0^\circ, 9^\circ, 180^\circ$ and 189° on Station 3, and $\phi = 0^\circ - 36^\circ$ and $153^\circ, 162^\circ, 180^\circ - 198^\circ$ on Station 9 at $Re = 0.7 \times 10^6$; $\phi = 189^\circ$ on Stations 3 and 9 for $Re = 0.9 \times 10^6$.

To examine the mechanism for the reduction of maximum local side-force coefficient, Table 3 compares the wake angle $\Delta\theta_w$ and the local side-force coefficient C_{Yd} at $\phi = 324^\circ$ and Stations $3 - 9$ for various Reynolds numbers. The boundary-layer separation state is $\mathcal{LS}$ at $Re = 0.1 \times 10^6$, $\mathcal{LS} - \mathcal{TRS}$ at $Re = (0.3, 0.5) \times 10^6$

and $\mathcal{TRS}-\mathcal{TS}$ at $Re=(0.7,0.9)\times10^6$. The wake center lies on the starboard side of the section for all cases. No disagreement between the wake asymmetry and the pressure asymmetry occurs throughout. The wake angle is large for $\mathcal{LS}$ and small for $\mathcal{TRS}$. Under a given free-stream Reynolds number the wake angle decreases along the cone length downstream. Small wake angle yields weak wake vortices and low side force. The significant reduction of the maximum local side-force coefficient at $Re=(0.7,0.9)\times10^6$ are caused by the frequent appearance of the transitional separation state, $\mathcal{TRS}$.

Table 3. Comparison of wake angle $\Delta\theta_w$ and corresponding C_{Yd} at $\phi=324^\circ$, Stations $3-9$ and various Reynolds numbers.

$Re/10^6$	*Station*													
	3		4		5		6		7		8		9	
	$\Delta\theta_w$	C_{Yd}	$\Delta\theta_w$	C_{Yd}	$\Delta\theta_w$	C_{Yd}	$\Delta\theta_w$	C_{Yd}	$\Delta\theta_w$	C_{Yd}	$\Delta\theta_w$	C_{Yd}	$\Delta\theta_w$	C_{Yd}
0.1	160°	−0.71	160°	−0.67	160°	−0.67	160°	−0.67	160°	−0.63	160°	−0.63	160°	−0.63
0.3	160°	−0.67	160°	−0.63	160°	−0.63	130°	−0.62	130°	−0.60	130°	−0.57	130°	−0.56
0.5	140°	−0.68	120°	−0.65	120°	−0.64	120°	−0.63	120°	−0.60	120°	−0.58	100°	−0.56
0.7	110°	−0.63	100°	−0.60	90°	−0.53	90°	−0.50	90°	−0.43	90°	−0.36	90°	−0.28
0.9	120°	−0.63	100°	−0.58	90°	−0.53	80°	−0.44	80°	−0.38	80°	−0.30	80°	−0.18

V. $C_{Yd}(x/L)$ at Various Reynolds Numbers

Figure 13 gives the local side-force coefficients C_{Yd} versus x/L for various Reynolds numbers, (a) $\phi=0^\circ$, (b) $\phi=90^\circ$, (c) $\phi=180^\circ$, and (d) $\phi=270^\circ$. In Fig. 13 (b) $C_{Yd}(x/L)$ for $Re=0.1\times10^6$ differs from others. From Figs. 6 and 7 $\phi=90^\circ$ is a crossover point on the square-wave curve of $C_{Yd}(\phi)$. Micro surface imperfections of the model would penetrate the thin laminar boundary layer at this low Reynolds number to trigger the early crossover. $\phi=270^\circ$ is a maximum point on the square-wave curve of $C_{Yd}(\phi)$. Fig. 13 (d) shows that C_{Yd} decreases as Reynolds number increases. This is caused by the wake-angle reduction similar to the point of $\phi=324^\circ$ as elaborated in Table 3. In Fig. 13 (a) $C_{Yd}(x/L)$ for $Re=0.7\times10^6$ differs from others remarkably. This is related to the irregular value on the square-wave curve of $C_{Yd}(\phi)$ in Figs. 6 and 7 and is explained below. In Fig. 13 (c) the deviation for $Re=(0.7,0.9)\times10^6$ is also related to the corresponding irregular value.

Figure 14 compares the pressure distributions at Stations 3 and 9 and $\phi=0^\circ$ for Reynolds numbers of 0.3×10^6 and 0.7×10^6. At $Re=0.3\times10^6$ the boundary-layer separation state is $\mathcal{LS}-\mathcal{TRS}$ and the second suction peak stays on the starboard side at Stations 3 and 9. At $Re=0.7\times10^6$ the separation state is $\mathcal{TRS}-\mathcal{TRS}$ and $\mathcal{TS}-\mathcal{TRS}$ at Station 3 and Station 9, respectively. The second suction peak occurs on the starboard and port side at Station 3 and Station 9, respectively.

Table 4. Comparison of meridian angle of the wake center θ_w and the corresponding C_{Yd} at $\phi=0^\circ$, $Re=(0.3,0.7,0.9)\times10^6$.

$Re/10^6$	*Station*													
	3		4		5		6		7		8		9	
	θ_w	C_{Yd}	θ_w	C_{Yd}	θ_w	C_{Yd}	θ_w	C_{Yd}	θ_w	C_{Yd}	θ_w	C_{Yd}	θ_w	C_{Yd}
0.3	150°	+0.54	150°	+0.54	150°	+0.54	150°	+0.54	155°	+0.54	150°	+0.54	150°	+0.52
0.7	<u>185°</u>	+0.17	175°	+0.11	175°	+0.04	<u>175°</u>	−0.01	<u>180°</u>	−0.05	<u>180°</u>	−0.09	<u>180°</u>	−0.10
0.9	165°	+0.52	165°	+0.51	155°	+0.50	155°	+0.46	155°	+0.43	160°	+0.39	160°	+0.38

Table 4 compares the meridian angle of the wake center θ_w and the corresponding local side-force coefficient, C_{Yd} at Stations $3-9$ and $\phi=0^\circ$ for $Re=(0.3,0.7,0.9)\times10^6$, where the underline denotes disagreement between the separation asymmetry and the pressure asymmetry. At $Re=0.3\times10^6$ the separation state remains $\mathcal{LS}-\mathcal{TRS}$ throughout, the wake angle $\Delta\theta_w\approx120^\circ$, and θ_w and C_{Yd} are almost invariant on Stations $3-9$. The wake asymmetry agrees with the pressure asymmetry throughout. At $Re=0.7\times10^6$ the separation state remains $\mathcal{TRS}-\mathcal{TRS}$ on Stations $3-7$, and changes to $\mathcal{TS}-\mathcal{TRS}$ at Stations 8 and 9. $\Delta\theta_w\approx90^\circ$. The separation asymmetry disagrees with the pressure asymmetry at most Stations. $C_{Yd}(x/L)$

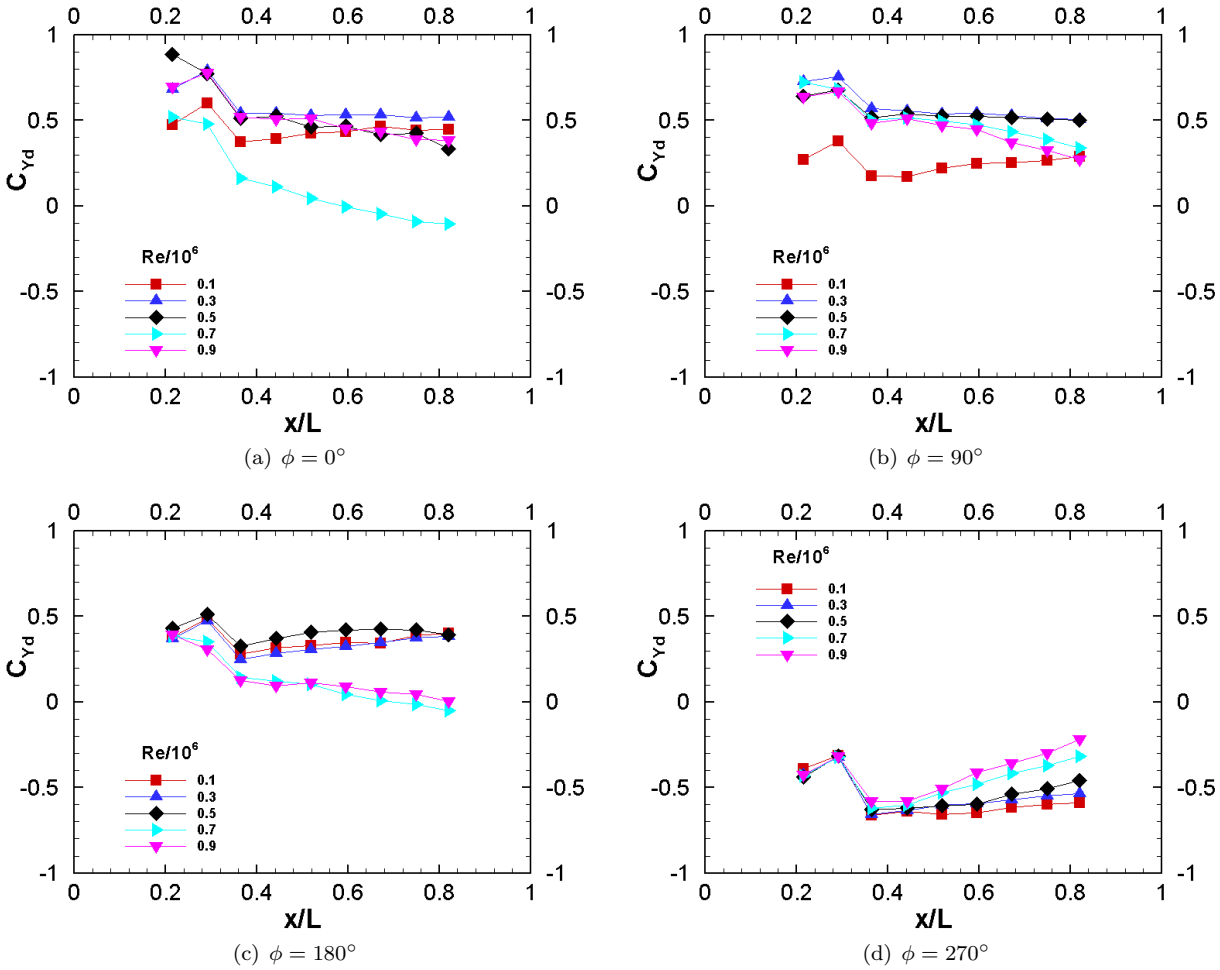

(a) $\phi = 0°$ (b) $\phi = 90°$

(c) $\phi = 180°$ (d) $\phi = 270°$

Figure 13. Local side-force coefficients vs. x/L at different ϕ for various Reynolds numbers.

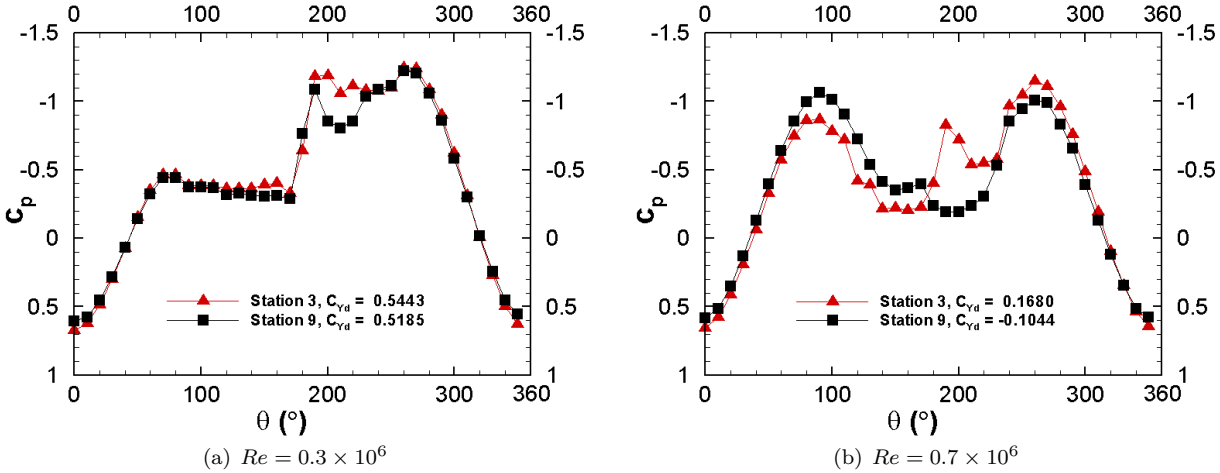

(a) $Re = 0.3 \times 10^6$ (b) $Re = 0.7 \times 10^6$

Figure 14. Comparison of pressure distributions at Stations 3 an 9, $\phi = 0°$.

is remarkably lower than others. At $Re = 0.9 \times 10^6$ the separation state remains $\mathcal{TRS} - \mathcal{TS}$ on Stations $3 - 5$, changes to $\mathcal{TRS} - \mathcal{TRS}$ at Stations $6 - 8$ and changes to $\mathcal{TS} - \mathcal{TS}$ at Station 9. $\Delta\theta_w$ decreases from 110° to 80°, but the separation asymmetry agrees througout. $C_{Yd}(x/L)$ has no distinct behavior. The low-value behavior of $C_{Yd}(x/L)$ at $Re = 0.7 \times 10^6$ and $\phi = 0°$ would be caused by the disagreement between the separation asymmetry and the pressure asymmetry.

Table 5 compares the meridian angle of the wake center θ_w and the corresponding local side-force coefficient, C_{Yd} at Stations $3 - 9$ and $\phi = 180°$ for $Re = (0.3, 0.7, 0.9) \times 10^6$, where the underline denotes disagreement between the separation asymmetry and the pressure asymmetry. The low-value behavior of $C_{Yd}(x/L)$ at $Re = 0.7 \times 10^6$ and $\phi = 180°$ would be caused by the disagreement between the separation asymmetry and the pressure asymmetry. At $Re = 0.9 \times 10^6$ and $\phi = 180°$ the wake angle is small, $\Delta\theta_w \approx 90°$, but no separation-pressure asymmetry disagreement occurs. The exact reason for the low-value behavior of $C_{Yd}(x/L)$ is unclear.

Table 5. Comparison of meridian angle of the wake center θ_w and the corresponding C_{Yd} at $\phi = 180°$, $Re = (0.3, 0.7, 0.9) \times 10^6$.

$Re/10^6$	*Station*													
	3		4		5		6		7		8		9	
	θ_w	C_{Yd}	θ_w	C_{Yd}	θ_w	C_{Yd}	θ_w	C_{Yd}	θ_w	C_{Yd}	θ_w	C_{Yd}	θ_w	C_{Yd}
0.3	175°	+0.26	175°	+0.29	170°	+0.32	170°	+0.33	170°	+0.36	170°	+0.37	150°	+0.38
0.7	<u>190°</u>	+0.14	175°	+0.12	175°	+0.12	175°	+0.04	<u>180°</u>	+0.02	<u>175°</u>	−0.02	<u>175°</u>	−0.05
0.9	170°	+0.13	175°	+0.10	175°	+0.12	175°	+0.09	170°	+0.06	170°	+0.04	170°	+0.01

VI. Abrupt Sign-Reversal of $C_{Yd}(\phi)$ at Various Reynolds Numbers

As shown in Fig. 6, the local side-force coefficient undergos abrupt sign reversal. It happens at about the same roll angle for all stations and all of the Reynolds numbers. Fig. 15 compares the pressure distributions of Station 3 at $\phi = 99°$ and 108° for $Re = 0.3 \times 10^6$ and $Re = 0.7 \times 10^6$. At $\phi = 99°$, a second suction peak occurs on the starboard side. After a roll increment of 9°, the second suction peak shifts from starboard side to the port side, and the wake region rotates clockwise accordingly. Table 6 compares C_{Yd}, separation state, wake angle $\Delta\theta_w$ and meridian angle of wake center θ_w at $\phi = 99°$ and 108°. At $Re = 0.3 \times 10^6$ the boundary-layer seoaration state is $\mathcal{LS} - \mathcal{LS}$ and the wake angle is 170° before and after abrupt change of C_{Yd}. At $Re = 0.7 \times 10^6$ the state stays $\mathcal{TRS} - \mathcal{TRS}$ and the wake angle stays 120°. For the two Reynolds numbers, the boundary-layer separation states are different and the wake angles are unequal, but the pressure asymmetries undergo the same reversal. Similar features at the abrupt sign-reversal of local side force are observed for all other Reynolds numbers and stations. Evidently, the pressure-asymmetry change and the sign reversal of local side force on the cone forebody is produced by inviscid hydrodynamic instability of the separation vortices in the leeward side of the cone for all of the Reynolds numbers rather than the separation variation.

Table 6 Comparison of C_{Yd}, separation state, wake angle $\Delta\theta_w$ and meridian angle of wake center θ_w at $\phi = 99°$ and 108° at Station 3.

$Re/10^6$	$\phi = 99°$				$\phi = 108°$			
	C_{Yd}	*State*	$\Delta\theta_w$	θ_w	C_{Yd}	*State*	$\Delta\theta_w$	θ_w
0.3	0.27	$\mathcal{LS} - \mathcal{LS}$	170°	174°	−0.66	$\mathcal{LS} - \mathcal{LS}$	170°	183°
0.7	0.40	$\mathcal{TRS} - \mathcal{TRS}$	120°	169°	−0.58	$\mathcal{TRS} - \mathcal{TRS}$	120°	188°

VII. Comparison of Pressure Distributions Corresponding to Equal C_{Yd} at Various Reynolds Numbers

Even though the local side force varies randomly with roll orientation, there exist asymmetric features independent of roll angle. One of such features is the existence of a constant maximum C_{Yd} independent of roll at a given station as shown in Fig. 6. Another feature is that the local side force is associated with a

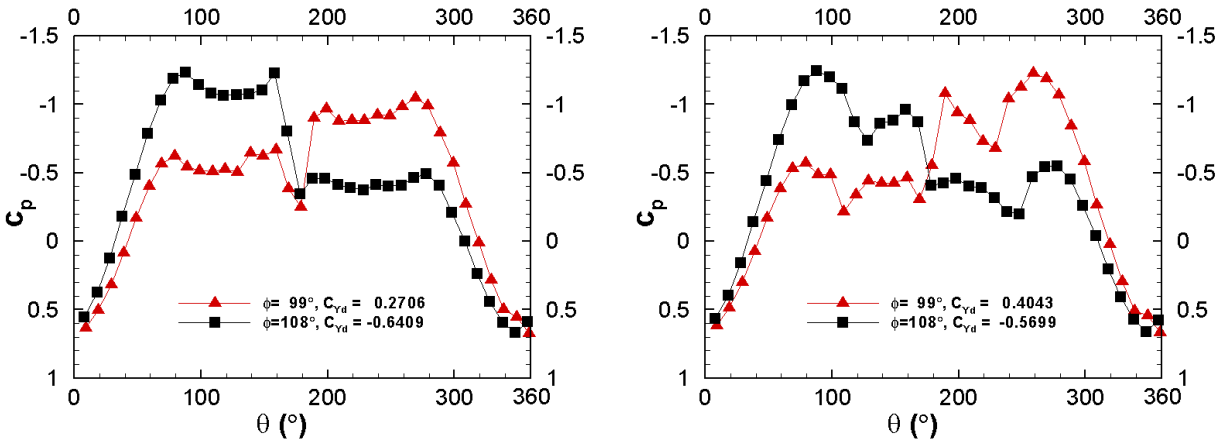

(a) $Re = 0.3 \times 10^6$ (b) $Re = 0.7 \times 10^6$

Figure 15. Comparison of pressure distributions at $\phi = 99°$ and $108°$ at Station 3.

unique pressure distribution independent of roll at a given station. This has been shown for $Re = 0.3 \times 10^6$ and 0.9×10^6 in Refs. 13 and 12, respectively. The association of C_{Yd} with unique $C_p(\theta)$ for the rest Reynolds numbers is studied here.

Figure 16 compares the two pressure distributions corresponding to equal local side force coefficient occurring at two different roll angles for various Reynolds numbers at Station 3. Table 7 compares roll angle, separation state, wake angle $\Delta\theta_w$ and meridian angle of wake center θ_w of the two pressure distributions corresponding to equal local side force at Station 3 shown in Figure 16, where the underline denotes the the separation asymmetry disagrees with the pressure asymmetry. From Fig. 16 the pressure distributions corresponding to the equal local side-force coefficient at the two different roll angles are almost identical at $Re = 0.1 \times 10^6$ and 0.5×10^6, but deviations appear at $Re = 0.7 \times 10^6$. The deviations are significant in the wake region because the separation states on the two sides of the model are altered by the roll-angle change at this transitional Reynolds number.

Table 7 Comparison of roll angle, separation state, wake angle $\Delta\theta_w$ and meridian angle of wake center θ_w of the two pressure distributions corresponding to equal C_{Yd} at Station 3.

		$(Pressures)_1$				$(Pressures)_2$			
$Re/10^6$	C_{Yd}	ϕ	$State$	$\Delta\theta_w$	θ_w	ϕ	$State$	$\Delta\theta_w$	θ_w
0.1	0.46	81°	$\mathcal{LS} - \mathcal{LS}$	160°	171°	207°	$\mathcal{LS} - \mathcal{LS}$	160°	167°
0.5	0.50	72°	$\mathcal{LS} - \mathcal{TRS}$	140°	152°	198°	$\mathcal{LS} - \mathcal{TRS}$	140°	158°
0.7	0.14	9°	$\mathcal{TRS} - \mathcal{TRS}$	90°	<u>184°</u>	18°	$\mathcal{TS} - \mathcal{TRS}$	80°	148°
0.7	−0.67	117°	$\mathcal{TS} - \mathcal{TRS}$	120°	187°	342°	$\mathcal{TRS} - \mathcal{TS}$	90°	197°

In Fig. 16 (c), as the roll angle varies from 9° to 18°, the boundary-layer separation state on the starboard side remains $\mathcal{TRS}$ but that on the port side changes from initially being $\mathcal{TRS}$ to finally $\mathcal{TS}$. This is triggered by the micro surface imperfections brought in by the roll of 9°. Since the separation occurs earlier on the port side due to $\mathcal{TS}$, the wake center shifts from the starboard side to the port side, and the wake asymmetry changes from disagreeing with the pressure asymmetry to agreeing. The second suction peak initially located on the starboard side shifts to the other side of the incidence plane. However, the asymmetry of the corresponding pressure distributions remains unchanged. It indicates that the second suction is still induced by the vortex core separated from the starboard side. For a $3.5D$-ogive nose ($\epsilon = 16.3°$) at transitional Reynolds number of 0.8×10^6 and $\alpha = 55°$, Keener[5] observed that the asymmetry in the oil-flow pattern becomes so large that the primary vortex close to the surface actually crosses over the top centerline.

From Fig. 16 (d), the separation state is $\mathcal{TS} - \mathcal{TRS}$ at $\phi = 117°$ and $\mathcal{TRS} - \mathcal{TS}$ at $\phi = 342°$. The separation state changes hand for the two roll angles. As the flow on the port side has higher speed than on

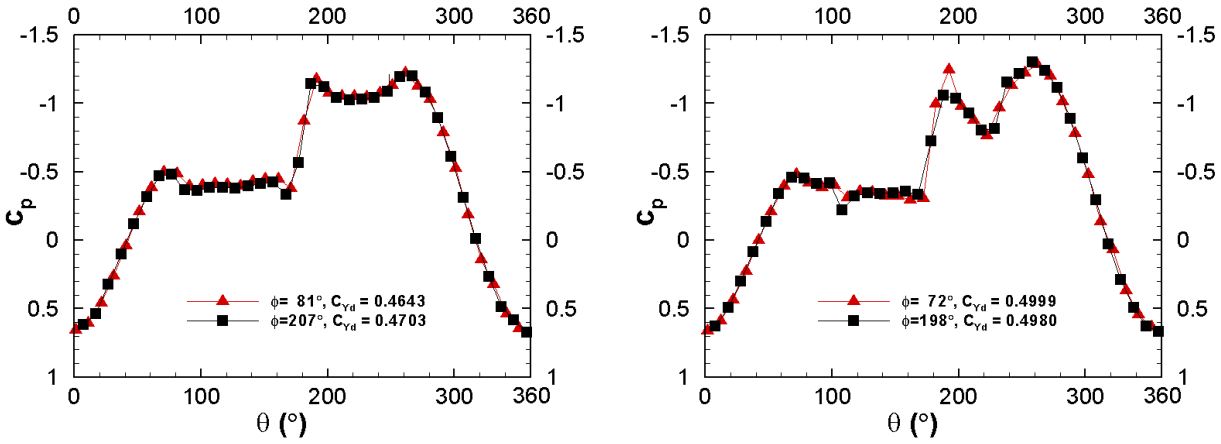

(a) $Re = 0.1 \times 10^6$ (b) $Re = 0.5 \times 10^6$

(c) $Re = 0.7 \times 10^6$ (d) $Re = 0.7 \times 10^6$

Figure 16. Comparison of pressures corresponding to equal C_{Yd} at different ϕ, Station 3, and various Reynolds numbers.

the starboard side, the state change on the port side has dominant effect. The wake angle decreases from 120° to 90° caused by the separation delay on the port side due to $\mathcal{TRS}$ and the original second suction peak of the port side becomes faint. However, the pressure distribution remains essentially unchanged. Disappearance of the second suction peak in asymetric pressure distribution in transitional flow was also reported by Lamont[4] for a $2D$-ogive cylinder ($\epsilon = 28.1°$) on the nose-cylinder junction at $\alpha = 55°$ in his Fig. 11.

Even though the boundary-layer separation position on either side of the cone forbody may vary significantly at $Re = 0.7 \times 10^6$, the deviations in the pressure distributions corresponding to equal local side force are limited. Thus, the governing mechanism for all of the Reynolds numbers is inviscid hydrodynamic instability of the separation vortices rather than alteration of the boundary-layer separation state. Since the unique pressure distribution associated with a local side force at a given station is independent of roll angle, it can be applied for cones of the same apex angle under the same flow conditions. This has been verified in Ref. 12 by comparing with Fiddes' test results.[9]

VIII. Overall Force- and Moment-Coefficiants at Various Reynolds Numbers

The overall forces and moments acting on the cone are calculated from integrating the measured pressures at the nine stations. The longitudinal length of the cone from the apex to the base is divided into nine elements by the eight mid points between the neighboring stations. On each element, the pressure distributions are assumed to be constant along the same meridian line. The overall side- and normal-force coefficient, C_{Y0} and C_{N0} are defined by the base area of the cone S. The yawing- and pitching-moment coefficients, C_n and C_m are defined by S and the base diameter, D. The moment center is positioned at the base of the cone. Figure 17 presents the overall side-force, overall normal-force, yawing-moment, and pitching-moment coefficients versus roll angle at various Reynolds numbers. The variation of the lateral force and moment versus roll angle have similar square-wave curves, and the maximum positive and the maximum negative values have about the same magnitude for each Reynolds number. At the transitional Reynolds numbers, $Re = (0.7, 0.9) \times 10^6$, the maximum side force and yawing moment are reduced, and irregular values occur at the roll angles listed in Table 1. The longitudinal force and moment are nearly constant over entire roll orientation for all Reynolds numbers and of the same order of magnitude as the extremes of the corresponding lateral force and moment.

Figure 18 presents the extremes of the overall force and moment coefficients over entire orientation versus Reynolds number. The extremes of the overall side force are reduced in the transitional separation regime, but not to such a deep level as that for a $2D$-ogive and $4D$-cylinder combination at $\alpha = 55°$ shown by Lamont[4] in his Fig. 8. The reason for the deviation may be that only forebody is counted in the present results. A force measurements were conducted by Keener et al.[14] They gave forces and moments measured at various Reynolds numbers, but at only one roll orientation. Their results are reproduced in Fig. 18, and lie well between the present extremes, which confirms the present results and supports the belief that the extremes are independent of micro surface imperfections of models.

IX. Conclusions

Pressure measurements at 9 stations over a 20° cone forebody at 35° angle of attack, zero sideslip and all roll angles in 9° intervals were performed in a low-turbulence, low-speed, large-scale wind tunnel with a rigid support. The tests encompassed a range of free-stream Reynolds numbers based on the cone-base diameter (0.1×10^6 to 0.9×10^6) and Mach numbers ($0.03 - 0.24$). Separation state of the boundary layer on the two sides of the cone is inferred from the measured pressures. The experimental setup is verified with the measured pressures at zero incidence. The results are confirmed by test data in the literature.

Effects of Reynolds number on asymmetric force are evident at free-stream Reynolds numbers of $(0.7, 0.9) \times 10^6$. The extremes of the square-wave curve of the (local and overall) side-force coefficient versus roll angle are reduced, which results from late boundary-layer separation or samll wake angle ($80° - 90°$). The pressure distributions experience abnormal changes: the second suction peak originated from one side of the cone may cross the centerline to the other side or faint or even disappear, while the direction of the local side force remains unchanged. Irregular values of the side force appear at a few roll angles. This is caused by the disagreement between the separation asymmetry and the pressure asymmetry besides the small wake

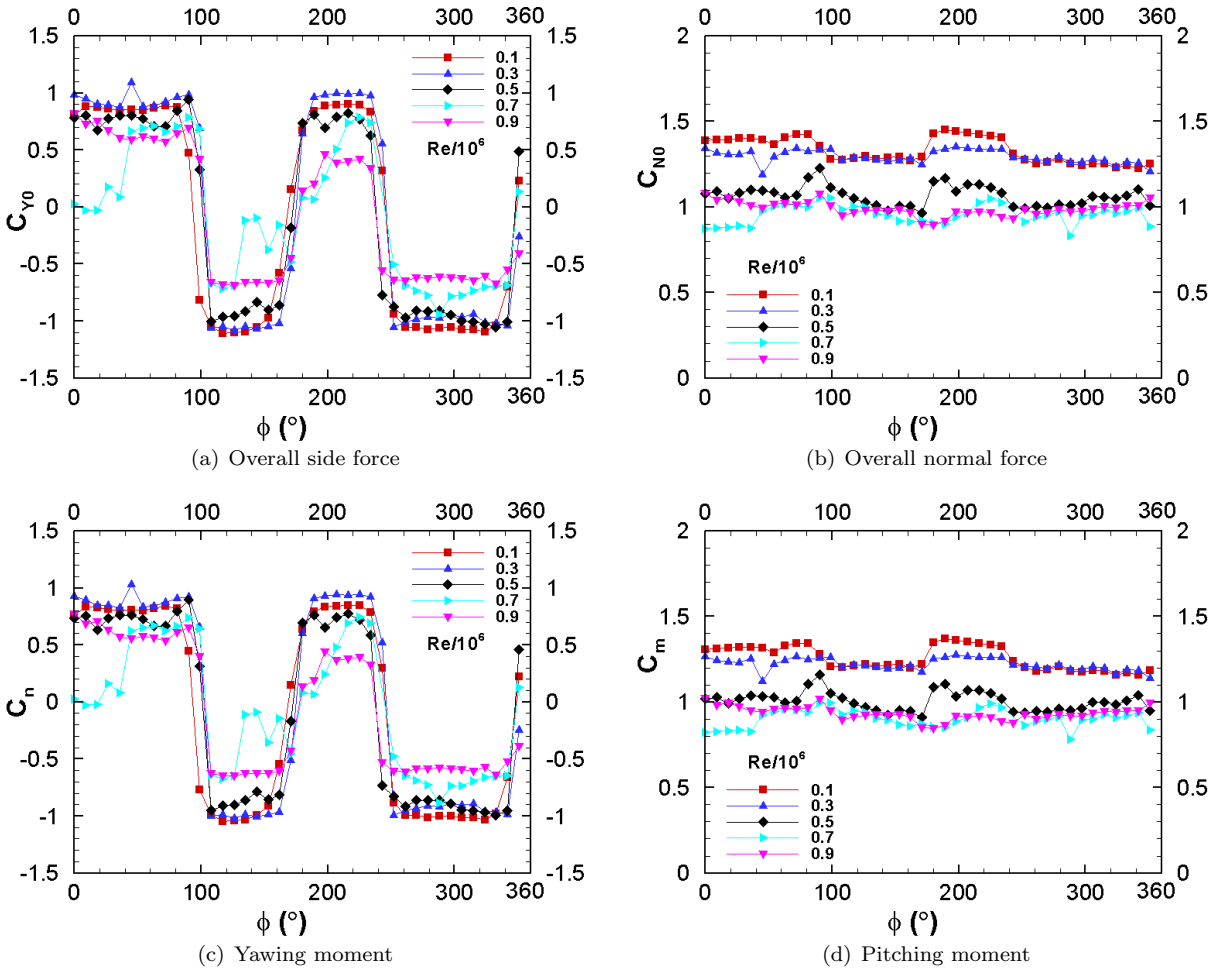

(a) Overall side force

(b) Overall normal force

(c) Yawing moment

(d) Pitching moment

Figure 17. Overall force- and moment-coefficients vs. ϕ at various Reynolds numbers.

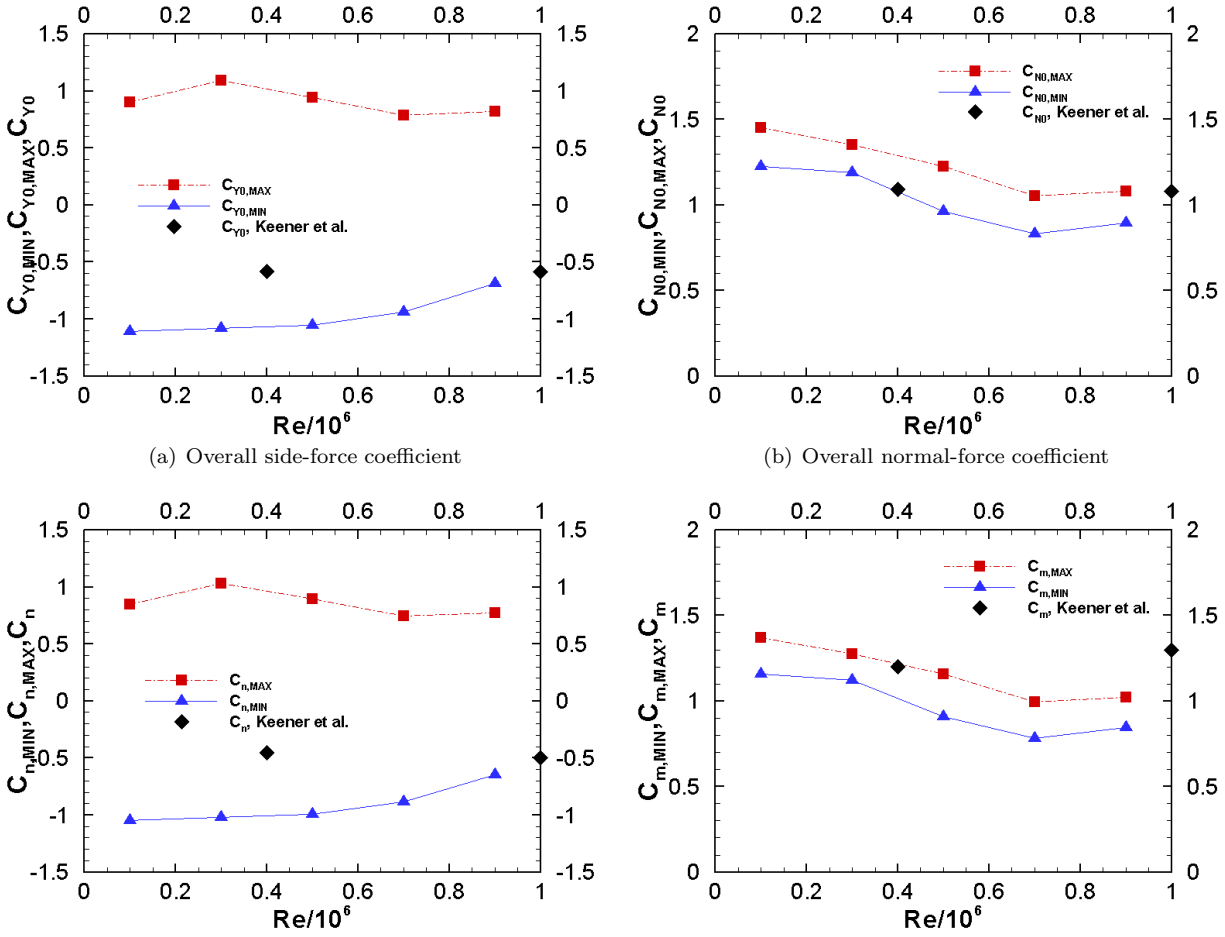

(a) Overall side-force coefficient

(b) Overall normal-force coefficient

(c) Yawing-moment coefficient

(d) Pitching-moment coefficient

Figure 18. Extremes of Overall force and moment coefficients vs. Re compared with Keener et al.[14]

angle. The origin for these effects is the different transition mechanisms of boundary layer on either side of the cone.

There exist important asymmetry features which are valid for all of the Reynolds numbers. The local side-force coefficient varies with roll angle in a pattern of square wave with positive and negative extremes of equal magnitude at a given section of the cone. It experiences zero crossings at about the same roll angles for all sections. The pressure distributions corresponding to equal local side force at different roll angles at a given section and a given Reynolds number are essentially identical but with some minor deviations at the transitional Reynolds numbers. The forgoing features support the proposition that the principal cause of force asymmetry is the hydrodynamic instability of the inviscid vortex flow in the leeward side of the cone. Asymmetry in boundary-layer separation, especially at transitional Reynolds numbers, may alter the pressure distribution.

Acknowledgments

The present work is supported by the Foundation for Fundamental Research of the Northwestern Polytechnical University, NPU-FFR-W018101. The authors are grateful to Professor Xueying Deng of Beijing University of Aeronautics and Astronautics for using the pressure-transducer system.

References

[1]Allen, H.J., and Perkins, E.W., "Characteristics of flow over inclined bodies of revolution," NACA RM-A50L07, 1951.

[2]Haines, A.B., "Scale effects on aircraft and weapon aerodynamics," AGARD-AG-323, July 1994.

[3]Munro, C.D., Krus, P., and Jouannet, C., "Implications of scale effect for the prediction of high angle of attack aerodynamics," *Progress in Aerospace Sciences*, Vol. 41, 2005, pp. 301–322.

[4]Lamont, P.J., "Pressure around an inclined ogive cylinder with laminar, transitional, or turbulent separation," *AIAA Journal*, Vol. 20, No. 11, Nov. 1982, pp. 1492–1499.

[5]Keener, E.R., "Flow-separation patterns on symmetric forebodies" NASA TM 86016, 1986.

[6]Hall, R.M., "Influence of Reynolds number on forebody side forces for 3.5-diameter tangent-ogive bodies," AIAA-87-2274, Jun. 1987

[7]Poll, D.I.A., "On the effects of boundary-layer transition on a cylindrical afterbody at incidence in low-speed flow," *The Aeronautical Journal*, Oct. 1986, pp. 315–327.

[8]Moskovitz, C.A., Hall, R.M., and DeJarnette, F.R., "New device for controlling asymmetric flowfields on forebodies at large alpha," *Journal Aircraft*, Vol. 28, No. 7, Jul. 1991, pp. 456–462.

[9]Fiddes, S., "Separated flow about cones at incidence–theory and experiment," *Proceedings of Symposium on Studies of Vortex Dominated Flow*, NASA/LRC, 1985, pp. 285–310.

[10]Meng, S., Jia, C. ,Qiao, Z., Gao, C., Luo, S., and Liu, F., "Development of flow asymmetry over a 20-degree circular cone at low speed," AIAA Paper 2007-4118, June 2007.

[11]Hall, R.M., "Forebody and missile side forces and the time analogy," AIAA-87-0327, Jan. 1987.

[12]Jia, C., Meng, S., Qiao, Z., Gao, C., Luo, S., and Liu, F., "Pressure around a 20-degree circular cone at 35-degree angle of attack and low speed," AIAA Paper 2007-4453, June 2007.

[13]Meng, S., Jia, C. ,Qiao, Z., Gao, C., Luo, S., and Liu, F., "Association of local side force with pressures over a slender circular cone," Submitted to AIAA Applied Aerodynamics Conference, 18-21 Aug 2008 Honolulu, HI.

[14]Keener, E., Chapman, G., Cohen, L., and Taleghani, J., "Side forces on Forebodies at high angles of attack and Mach numbers from 0.1 to 0.7: two tangent ogives, paraboloid and cone," NASA TM X-3438, Feb. 1977.